

# Nonsaturating magnetoresistance, anomalous Hall effect, and magnetic quantum oscillations in the ferromagnetic semimetal PrAlSi

Meng Lyu,<sup>1,2</sup> Junsen Xiang,<sup>1</sup> Zhenyu Mi,<sup>1</sup> Hengcan Zhao,<sup>1,2</sup> Zhen Wang,<sup>1,2</sup> Enke Liu,<sup>1,2,3</sup>  
Genfu Chen,<sup>1,2,3</sup> Zhian Ren,<sup>1,2,3</sup> Gang Li,<sup>1,2,3</sup> and Peijie Sun<sup>1,2,3,\*</sup>

<sup>1</sup>Beijing National Laboratory for Condensed Matter Physics, Institute of Physics, Chinese Academy of Sciences, Beijing 100190, China

<sup>2</sup>School of Physical Sciences, University of Chinese Academy of Sciences, Beijing 100049, China

<sup>3</sup>Songshan Lake Materials Laboratory, Dongguan, Guangdong 523808, China



(Received 27 November 2019; revised 28 May 2020; accepted 5 August 2020; published 21 August 2020)

We report a comprehensive investigation of the structural, magnetic, transport, and thermodynamic properties of single crystal PrAlSi, in comparison to its nonmagnetic analog LaAlSi. PrAlSi exhibits a ferromagnetic transition at  $T_c = 17.8$  K which, however, is followed by two weak phase transitions at lower temperatures. The two reentrant magnetic phases can be suppressed by a small magnetic field of about 0.4 T and are proposed to be spin glasses or ferromagnetic cluster glasses based on dc and ac magnetic susceptibilities. Both the two compounds reveal large, nonsaturating magnetoresistance as a function of field. While Shubnikov-de Haas oscillations are absent in LaAlSi, they are clearly observed below about 25 K in PrAlSi, with an unusual temperature dependence of the dominating oscillation frequency  $F$ . It increases from  $F = 18$  T at 25 K to  $F = 33$  T at 2 K, hinting at an emerging Fermi pocket upon cooling into the ordered phase. Specific-heat measurements indicate a non-Kramers magnetic doublet ground state and a small overall crystal electric field splitting of the  $\text{Pr}^{3+}$  multiplets of less than 100 K; Hall-effect measurements show a large anomalous Hall conductivity amounting to  $\sim 2000 \Omega^{-1} \text{cm}^{-1}$  below  $T_c$ . These results suggest that PrAlSi is a new system where a small Fermi pocket is strongly coupled to local-moment magnetism. Whether topological state is also involved remains an intriguing open problem.

DOI: [10.1103/PhysRevB.102.085143](https://doi.org/10.1103/PhysRevB.102.085143)

## I. INTRODUCTION

Exploring the physics of magnetic semimetals is becoming increasingly important for several reasons. The first is related to Weyl physics [1]. Since the discovery of nonmagnetic Weyl semimetals without space-inversion symmetry, such as TaAs (Ref. [2]), searching for magnetic topological semimetals with broken symmetries of both time reversal and space inversion also develops into an important research field [3], where the interplay between relativistic fermions and internal magnetism is expected [4]. On the other hand, magnetic semimetals are interesting themselves because of, for example, the spin-dependent electronic state and charge transport [5], which may lead to potential applications in spintronics [6]. Finally, magnetic semimetals frequently come into the focus of research in the context of Mott or Kondo physics, suited for exploring electron-correlated behaviors in low carrier-density systems. Such cases are realized in the correlated Dirac semimetal of perovskite  $\text{CaIrO}_3$  [7] and the Weyl Kondo semimetals  $\text{YbPtBi}$  [8] and  $\text{CeRu}_4\text{Sn}_6$  [9].

Recently, rare-earth based compounds  $\text{RAlX}$  ( $R = \text{La, Ce}$  and  $\text{Pr}$ ;  $X = \text{Si}$  and  $\text{Ge}$ ) attract considerable attention as potential candidates of Weyl semimetals [10–16]. They commonly reveal a certain type of long-range magnetic ordering when  $R$  is Ce or Pr and may crystallize in two alternative body-

centered tetragonal lattices [17]. One has space group  $I4_1md$  (No. 109), derived from the prototype  $\text{LaPtSi}$  (Ref. [18]). This type of structure is noncentrosymmetric and has a polar point group  $4mm$ . The other is derived from  $\alpha\text{-ThSi}_2$  of  $I4_1/amd$  space group (No. 141) that has a centrosymmetric point symmetry of  $4/mmm$ . In contrast to the distinct occupations of  $4a$  Wyckoff sites by Al and X atoms in the former, they occupy the  $8e$  site randomly in the latter case [19]. A detailed comparison of the two structures has been made in a recent paper [11]. Among the  $\text{RAlX}$  family, compounds with  $X = \text{Ge}$  have been relatively well investigated thus far, albeit with considerable controversies on the magnetic properties. For example, while  $\text{RAlGe}$  was theoretically predicted to be a ferromagnetic (FM) Weyl semimetal [10], experimentally  $\text{CeAlGe}$  was found to be either antiferromagnetic (AFM) [11,12] or FM [19] and  $\text{PrAlGe}$  either a spin glass [12] or a ferromagnet [13]. On the other hand, the silicide  $\text{RAl}_x\text{Si}_{2-x}$  with  $x \sim 1$  has also been investigated on the structure and magnetism [19–21], revealing controversial physical properties as well. Table I briefly compiles the previously reported structure and magnetism of  $\text{RAlX}$ .

In this paper, we focus on PrAlSi and report the single crystal synthesis, detailed investigations of its crystal structure, magnetic, transport, and thermodynamic properties. Note that the  $4f^2$  configuration of the  $\text{Pr}^{3+}$  ion, as confirmed for PrAlSi, is at the center of various exotic physical properties like magnetic ordering, metal-insulator transition and heavy fermion behavior of a variety of Pr-based intermetallics [22]. In order

\*pjsun@iphy.ac.cn

TABLE I. Crystal structure and magnetism of typical RAlX compounds reported in literature. Here NCS and CS denote the noncentrosymmetric LaPtSi type and the centrosymmetric  $\alpha$ -ThSi<sub>2</sub> type structure, respectively. Note that most compounds have a wide homogeneous range and are slightly off-stoichiometric. SG denotes spin glass.

RAlX	Structure and magnetism
CeAlGe	NCS/AFM [11,15]; CS/AFM [21]; CS/FM [19]
PrAlGe	NCS/SG [12]; NCS/FM [13,16]
CeAlSi	CS/FM [21]; CS/AFM [19]
PrAlSi	NCS/FM [16]; CS/FM Refs. [18,20] and this work

to investigate the  $4f$  contributions to the physical properties of PrAlSi, the corresponding nonmagnetic compound LaAlSi without  $f$  electron was also prepared and studied. Our structure analysis by single crystal x-ray diffraction reveals PrAlSi to be centrosymmetric, with random occupation of Al and Si atoms on the same crystallographic site and a slightly off-stoichiometric composition, see Table II.

By performing dc and ac magnetic measurements, we are able to construct a complicated magnetic phase diagram for PrAlSi, which includes not only a FM phase below  $T_C$  but two spin-glass-like reentrant magnetic transitions at  $T_{M1}$  and  $T_{M2}$  below  $T_C$ . Electrical resistivity measurements show large, nonsaturating magnetoresistance in magnetic field for both PrAlSi and LaAlSi. Specific heat measurements indicate a non-Kramers doublet ground state and a relatively small overall splitting (less than 100 K) of the Pr<sup>3+</sup> multiplets due to the crystal electric field (CEF). The latter effect largely enhances the magnetic entropy associated with the FM

TABLE II. Refinement results of crystal structure and atomic information obtained for PrAlSi at room temperature. The values of  $U_{ii}$  denote anisotropic displacement parameters in unit  $\text{\AA}^2$ . Here, two sets of refinement results based on centrosymmetric  $\alpha$ -ThSi<sub>2</sub> type (upper) and noncentrosymmetric LaPtSi type (lower) structures are compared, among which we adopt the former one because the latter reveals unusually large or even negative values of  $U_{ii}$  for Al and Si.

Refined chemical formula: PrAl <sub>1.13</sub> Si <sub>0.87</sub>								
Crystal structure: Tetragonal $\alpha$ -ThSi <sub>2</sub> type								
Space group: $I4_1/amd$ (No. 141)								
Lattice constants: $a = b = 4.2255 \text{ \AA}$ , $c = 14.534 \text{ \AA}$								
Atom	Wyck.	$x$	$y$	$z$	$U_{11}$	$U_{22}$	$U_{33}$	o.p.
Pr	4a	0.5	0.75	0.375	0.0069	0.0069	0.0050	1
Al	8e	0.5	0.25	0.2082	0.019	0.002	0.003	$\sim 0.6$
Si	8e	0.5	0.25	0.2082	0.019	0.002	0.003	$\sim 0.4$
Refined chemical formula: PrAl <sub>1.19</sub> Si <sub>0.81</sub>								
Crystal structure: Tetragonal LaPtSi type								
Space group: $I4_1md$ (No. 109)								
Lattice constants: $a = b = 4.2255 \text{ \AA}$ , $c = 14.534 \text{ \AA}$								
Atom	Wyck.	$x$	$y$	$z$	$U_{11}$	$U_{22}$	$U_{33}$	o.p.
Pr	4a	0.5	0.5	0.4162	0.0061	0.0061	0.0043	1
Al1	4a	0	0	0.4997	-0.0062	-0.0069	0.015	1
Si	4a	0	0.5	0.5835	0.058	0.0106	-0.007	$\sim 0.8$
Al2	4a	0	0.5	0.5835	0.058	0.0106	-0.007	$\sim 0.2$

order. Hall-effect measurements reveal a large anomalous Hall conductivity in the FM state, amounting to  $\sim 2000 \text{ \Omega}^{-1} \text{ cm}^{-1}$ . Finally, we also introduce the Shubnikov-de Haas (SdH) oscillations of  $\rho(B)$  observed from slightly above  $T_C$  down to  $T = 2 \text{ K}$  for PrAlSi. Intriguingly, the dominating oscillation frequency is strongly temperature dependent, changing from  $F = 18 \text{ T}$  at 25 K to  $F = 33 \text{ T}$  at 2 K. By contrast, no SdH oscillations can be observed for the nonmagnetic LaAlSi in the same temperature and field window. These results signify a small but considerably expanded Fermi surface in PrAlSi upon cooling into the FM phase, suggestive of a significant coupling of the local magnetism of Pr<sup>3+</sup> ions and the small Fermi pocket of  $s$  and  $p$  electrons [10].

## II. EXPERIMENTAL DETAILS

Single crystals of PrAlSi and LaAlSi were grown from high-temperature self flux using molten Al as solvent [20]. High purity chunks of cerium/lanthanum, silicon, and aluminum were loaded into an alumina crucible in the mole ratio 1:1:10 and further sealed in a quartz tube under high vacuum. The loaded quartz tube was slowly heated up to 1150 °C in 12 h, held at that temperature for 2 h in order to ensure a sufficient melting. It was then cooled down to 750 °C in 100 h and dwelled for 2 days. The excess Al was removed by centrifuging at 750 °C at the end of the growing process. Large mirrorlike plates of single crystal PrAlSi and LaAlSi, see inset of Fig. 1, were obtained. Trace of residual aluminium on the surface of the obtained single crystals was removed in dilute solution of NaOH.

To identify the crystal structure of PrAlSi, single crystal x-ray diffraction pattern was collected at room temperature by employing the Bruker D8 Venture diffractometer. The crystal structure was refined by full-matrix least-squares fitting on the structure factor  $F^2$  using the SHELXL-2014/7 program.

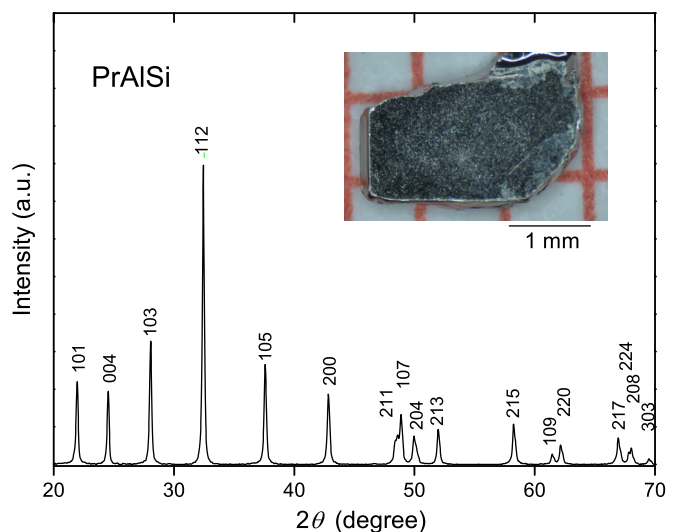


FIG. 1. Powder x-ray diffraction pattern of PrAlSi, with all Bragg peaks properly indexed. Note that both the  $\alpha$ -ThSi<sub>2</sub> and LaPtSi-type structures give the same index. Inset shows a photo image of the PrAlSi sample used for transport measurements, with  $c$  axis perpendicular to the as-grown plate.

The electrical resistivity and Hall effect were measured in the physical property measurement system (PPMS, Quantum Design) between 2 K and room temperature, using a sample of typical dimension  $0.3 \times 1 \times 3 \text{ mm}^3$ . The electrical current was applied within the tetragonal basal plane. Five-contact technique was employed for the Hall-effect measurements, where a weak field-even term due to longitudinal magnetoresistance was eliminated by scanning both negative and positive fields. The dc magnetic susceptibility and magnetization measurements were carried out in the MPMS-SQUID magnetometer, and the ac susceptibility was measured in various applied dc bias fields by employing the PPMS equipped with an ac susceptometer. The specific-heat measurements for both PrAlSi and LaAlSi were performed by a thermal-relaxation method.

### III. EXPERIMENTAL RESULTS AND DISCUSSION

#### A. Crystal structure

As already mentioned, two different but closely related crystal structures of LaPtSi and  $\alpha$ -ThSi<sub>2</sub> types are known for RAlX. The two structures differ in the sense that Al and X atoms can be either ordered and occupy two different Wyckoff  $4a$  sites or, alternatively, disordered and occupy the same  $8e$  site, see Ref. [11]. Powder x-ray diffraction pattern (Fig. 1) obtained for PrAlSi shows good agreement with other compounds of this family [11,12] and reveals no secondary phase. However, it can barely provide information on the difference of the two related structures.

Our single crystal x-ray diffraction analysis on PrAlSi supports a centrosymmetric symmetry with space group  $I4_1/amd$ . As shown in Table II (upper part), the best refinement indicates that Al and Si atoms occupy the same  $8e$  site randomly, with a composition PrAl<sub>1.13</sub>Si<sub>0.87</sub> that is in reasonable agreement with that obtained from energy-dispersive x-ray spectrum. The consequently determined lattice constants are  $a = 4.2255 \text{ \AA}$  and  $c = 14.534 \text{ \AA}$ . By contrast, intentionally assigning the noncentrosymmetric LaPtSi structure during the refinement will lead to unusually large or even negative values of anisotropic displacement parameters for Al and Si, see Table II (lower part). Excess of Al and deficiency of Si in RAlSi, as identified in both refinements, have so far been frequently detected in flux-grown samples from molten Al (Ref. [20]), which again points to the disordered nature of the Al and Si atoms in RAlSi. This situation is consistent with the previous report [20] of a large homogenous range of PrAl<sub>x</sub>Si<sub>2-x</sub> within the  $\alpha$ -ThSi<sub>2</sub> structure. In the presence of space-inversion symmetry, Weyl nodes cannot emerge naturally unless spin degeneracy is lifted through, e.g., breaking of time-reversal symmetry by applying external field or forming FM order. We note that a recent paper on PrAlSi shows strong signal of second-harmonic generation [16], an optical method that can resolve structural polarity. This result indicates a noncentrosymmetric structure of PrAlSi, contrary to our refinement. The reason behind this discrepancy most probably lies on the atomic disorder, which may be only partial, and the off-stoichiometry that is common to the RAlX family. Further investigation on lattice symmetry along this line is badly called for in order to clarify this discrepancy.

#### B. Magnetic properties

Figure 2 summarizes the experimental results of dc magnetic susceptibility measurements. In a small external magnetic field ( $B = 50 \text{ Oe}$ ) oriented along the  $c$  axis, a drastic increase of  $\chi(T)$  upon cooling, indicative of a FM transition, is observed in both the field-cooled (FC) and zero-field-cooled (ZFC)  $\chi(T)$  curves, see Fig. 2(a). The Curie temperature  $T_C = 17.8 \text{ K}$  is defined from the sharp minimum revealed in  $d\chi/dT(T)$ , as shown in Fig. 2(c) inset, and is consistent with previous reports on this compound [16,20]. The large values of  $\chi_{\parallel c}(T)$  relative to  $\chi_{\perp c}(T)$  already in paramagnetic phase manifest an Ising-type magnetic anisotropy. Note that the samples employed in Ref. [20] were PrAl<sub>1+x</sub>Si<sub>1-x</sub> with  $x = 0.15$  and  $0.19$ , similar in composition to our sample. At  $T < T_C$ , there appear two more weak anomalies at  $T_{M1} \simeq 16.5 \text{ K}$  and  $T_{M2} \simeq 9 \text{ K}$  [see dashed line in Fig. 2(a)], which can be better recognized in the  $d\chi(T)/dT$  curves [Fig. 2(c) inset] and by ac susceptibility to be shown below. Correspondingly, the FC and ZFC  $\chi(T)$  bifurcate significantly below  $T_C$ , indicative of spin-glass behavior below  $T_{M1}$  and  $T_{M2}$ . Occurrence of spin-glass phase below a FM/AFM transition is usually referred to as reentrant spin glass or cluster spin glass [23]. It has been frequently observed in materials with a certain type of magnetic frustration or atomic disorder, see, for example, Eu<sub>x</sub>Sr<sub>1-x</sub>S (Ref. [24]) and Mn<sub>3</sub>Sn (Ref. [25]). Similar thermal irreversibility of  $\chi(T)$  at  $T < T_C$  has also been observed for PrAlGe [12,13]. All three phase transitions of PrAlSi were also confirmed in  $\chi(T)$  measured with  $B \perp c$ , see Fig. 2(a) inset.

Shown in Fig. 2(b) are the  $T$ -dependent inverse susceptibilities  $1/\chi$  for both  $B \parallel c$  and  $B \perp c$ . From the linear variation of the Curie-Weiss behavior at  $T > 100 \text{ K}$ , the effective magnetic moment  $\mu_{\text{eff}}$  are estimated to be  $3.47$  and  $3.6 \mu_B$ , respectively, close to the free moment of the trivalent Pr ion,  $3.58 \mu_B$ . Reflecting the Ising-like magnetocrystalline anisotropy, the paramagnetic Weiss temperature  $\theta_p$  is strongly anisotropic, being  $28.9 \text{ K}$  for  $B \parallel c$  and  $-15.8 \text{ K}$  for  $B \perp c$ .

To shed light on the nature of the multiple magnetic phases, in Figs. 2(c) and 2(d) we show the  $\chi(T)$  curves recorded in different external fields ( $B \parallel c$ ) in FC and ZFC conditions, respectively. What can be readily recognized is a smooth decrease of  $T_{M2}$  upon increasing field in the FC  $\chi(T)$  measurements, see arrows in Fig. 2(c), where the variations of  $T_C$  and  $T_{M1}$  cannot be resolved due to their closeness in temperature. Meanwhile, the drastic decrease of the ZFC  $\chi(T)$  values below  $T_C$  is gradually suppressed upon increasing  $B$ , see Fig. 2(d). In Fig. 2(d) inset, we display the ZFC and FC  $\chi(T)$  curves measured in a relatively large field,  $B = 0.5 \text{ T}$ . There, the two  $\chi(T)$  curves become qualitatively similar, with no additional anomalies at  $T < T_C$ .

The reentrant spin-glass phases can be further probed by ac susceptibility. In Fig. 3(a) we show the real ( $\chi'$ ) and imaginary ( $\chi''$ ) components of the ac susceptibility measured as a function of temperature in an ac field of  $10 \text{ Oe}$  and frequency  $f = 333 \text{ Hz}$ . The curve of  $\chi'(T)$  shows a steep increase at  $T_C$  upon cooling, revealing a sharp minimum in  $d\chi'/dT$  [Fig. 3(b)]. Unlike typical ferromagnets,  $\chi'(T)$  does not drop quickly at  $T < T_C$  (Ref. [26]); instead, broad humps appear in  $\chi'(T)$  due to the weak phase transitions at  $T_{M1}$  and  $T_{M2}$ . This is better

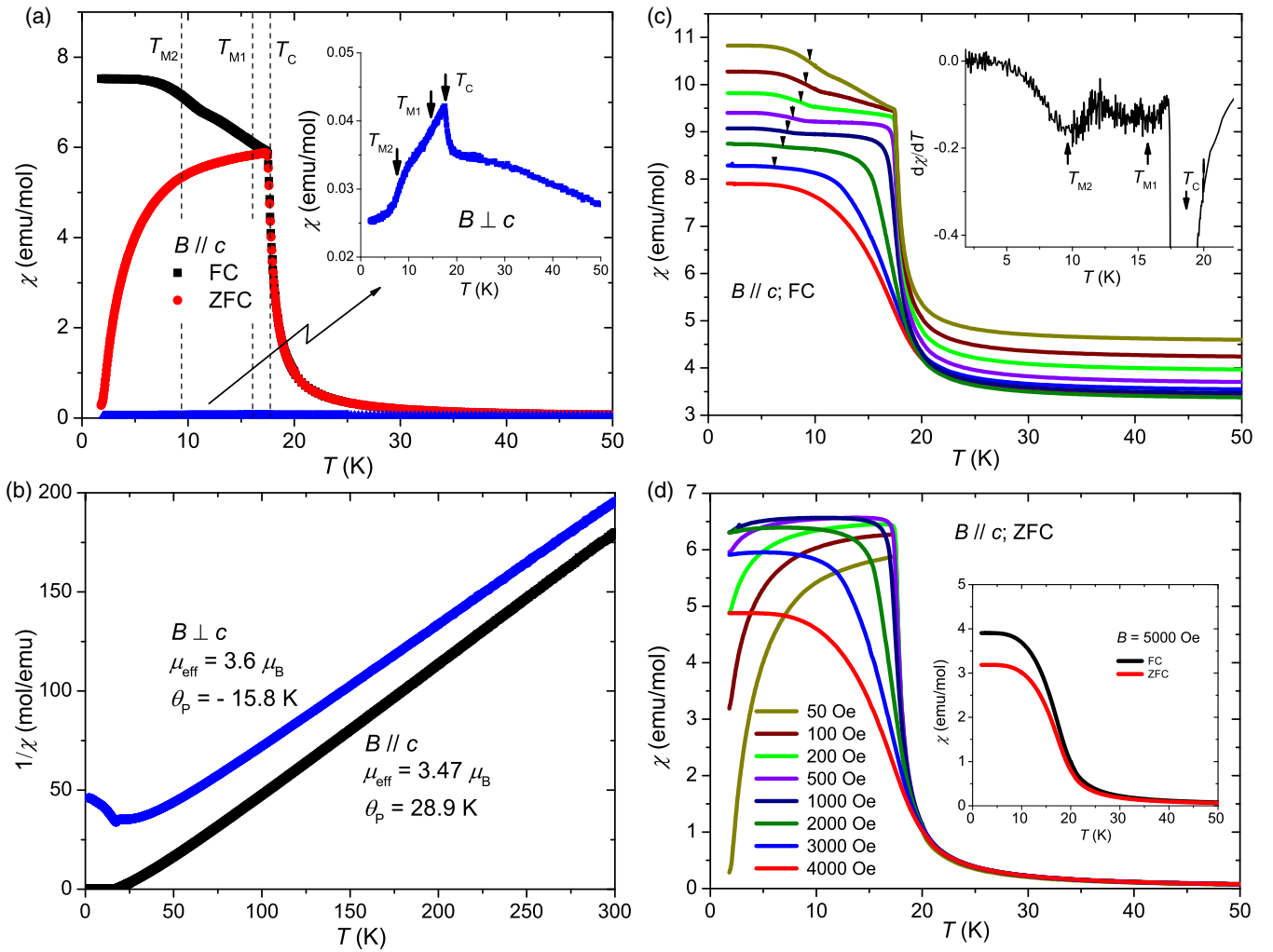


FIG. 2. (a) The dc magnetic susceptibility  $\chi(T)$  measured in ZFC and FC modes in an external field  $B = 50$  Oe. When  $B \parallel c$ , except for the FM transition at  $T_C = 17.8$  K, two subsequent weak anomalies at lower temperatures  $T_{M1}$  and  $T_{M2}$  are also observed. These anomalies can be better resolved in the derivative  $d\chi/dT$  shown in the inset of panel (c). Inset: A low-temperature closeup of  $\chi(T)$  measured with  $B \perp c$ . (b) The inverse susceptibility reveals linear  $T$  dependence from room temperature down to  $T \approx 100$  K, with a positive intercept at  $\theta_p = 28.9$  K and a negative one at  $\theta_p = -15.8$  K for  $B \parallel c$  and  $B \perp c$ , respectively. The obtained effective moments are close to that of the free  $\text{Pr}^{3+}$  ion. Panels (c) and (d) show FC and ZFC susceptibility  $\chi(T)$ , respectively, measured in varying dc fields oriented along  $c$ . Inset of (c) displays the derivative  $d\chi/dT$  of the FC  $\chi(T)$  curve measured in  $B = 50$  Oe. Inset of (d) displays the ZFC and FC  $\chi(T)$  results obtained for  $B = 5000$  Oe.

illustrated in the temperature derivative of  $\chi'(T)$  in Fig. 3(b). Accompanying the FM transition, enhanced values of  $\chi''(T)$  are also observed, forming a shoulder at  $T_{M1}$ . This behavior further indicates that the magnetic phase below  $T_{M1}$  is unlikely to be a (canted) AFM phase, where  $\chi''(T)$  is expected to vanish [26]. Similar shoulder in  $\chi''(T)$ , albeit weak, is also observed at  $T_{M2}$ .

As seen in Figs. 3(c) and 3(d), the values of  $T_{M1}$  and  $T_{M2}$  shift upward upon the increase of ac field frequency  $f$ , indicating spin-glass freezing within the two subsequent magnetic phases. This notion is consistent with the strong bifurcation of the ZFC and FC  $\chi(T)$  curves observed at low fields [Fig. 2(a)]. Figures 3(e) and 3(f) show the real component  $\chi'(T)$  and the corresponding temperature derivative  $d\chi'(T)/dT$  measured in varied external dc bias fields, respectively. With applying dc field, the magnetic transitions at  $T_C$  and  $T_{M1}$  separate from each other increasingly: The former slightly shifts to higher temperature, as expected for

a FM transition and the latter to lower temperature and is suppressed already in a small field of 0.4 T.

Figure 4 displays the isothermal magnetization  $M(B)$  for selected temperatures. At  $T < T_C$  and when  $B \parallel c$ , one observes a linear increase of  $M(B)$  until a metamagneticlike transition at a critical field  $B_c$  above which it flattens out. At  $T = 2$  K,  $M(B)$  saturates to  $3.4 \mu_B/\text{Pr}$  at  $B_c \approx 0.43$  T, a value close to the full moment of free  $\text{Pr}^{3+}$  ion ( $gJ = 3.2 \mu_B$ ). Magnetization measured at higher temperatures  $T = 10, 17,$  and  $20$  K shows that a similar saturated moment can be attained at higher fields (inset of Fig. 4). Polarization of the full local  $\text{Pr}^{3+}$  moment in relatively low field indicates that the splitting of its ninefold multiplets ( $J = 4$ ) in CEF, as well as the Kondo screening effect (if any) are rather weak as compared to the FM exchange interaction. The critical field  $B_c$ , marked by arrows in Fig. 4, decreases all the way with increasing temperature and vanishes at  $T \approx T_C$ . Characterizing the magnetic glassy state in field below  $B_c$  and

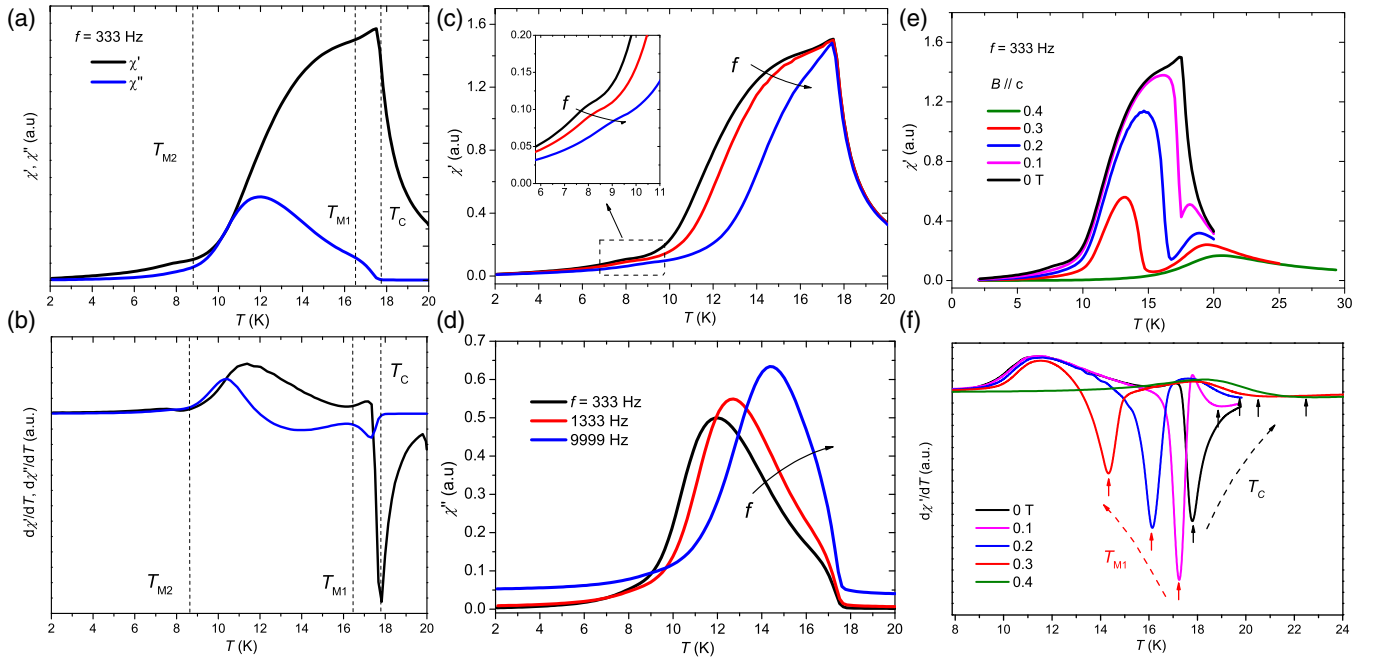


FIG. 3. The ac magnetic susceptibility of PrAlSi. (a) Real ( $\chi'$ ) and imaginary ( $\chi''$ ) components measured in an ac field of 10 Oe and  $f = 333$  Hz. The corresponding derivatives  $d\chi'/dT$  and  $d\chi''/dT$  are shown in panel (b). The FM transition at  $T_C$  and the two subsequent transitions at  $T_{M1}$  and  $T_{M2}$  are indicated by vertical lines, which mark the temperatures where  $d\chi'/dT$  assumes a minimum. (c), (d) Temperature dependence of  $\chi'(T)$  (c) and  $\chi''(T)$  (d) measured with various frequencies  $f$  in zero dc bias field. While  $T_C$  is robust to the change of ac field frequency, the anomalies corresponding to  $T_{M1}$  and  $T_{M2}$  shift to higher temperatures upon increasing  $f$ . (e), (f) Temperature dependence of  $\chi'(T)$  (e) and  $d\chi'/dT$  (f) in varying dc bias fields. It can be clearly seen from panel (f) that  $T_C$  increases, whereas  $T_{M1}$  decreases, with increasing dc field.

differing from typical ferromagnet, only a very weak hysteresis can be discerned at  $B < B_c$ , see  $M(B)$  for  $T = 2$  K. These

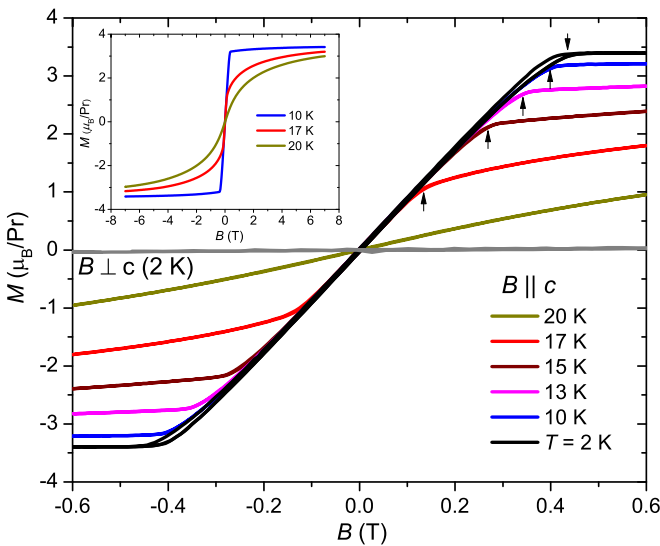


FIG. 4. Magnetization as a function of field ( $B // c$ ) for selected temperatures below and around  $T_C$ . Arrows indicate critical field  $B_c$  at which the low-field magnetic glassy phase changes to the high-field FM phase. Unlike typical ferromagnet, only a very weak hysteresis is visible, see the  $M(B)$  curve measured at  $T = 2$  K. Magnetization for  $B \perp c$  ( $T = 2$  K) is also shown in order to illustrate the large magnetic anisotropy. Inset shows  $M(B)$  measured up to a higher field of 7 T for  $T = 10$ , 17, and 20 K.

features indicate that the steplike magnetization at  $B_c$  does not represent spontaneous FM polarization but field-induced metamagneticlike transition from spin-glass to FM phase. The values of  $B_c$  obtained for different temperatures will be used to construct the magnetic phase diagram. Reversely, in the case of  $B \perp c$ ,  $M(B)$  measured at  $T = 2$  K (gray line) reveals negligible change up to 7 T, the largest magnetic field accessible in this work.

### C. Transport properties

Figure 5 displays the electrical resistivity  $\rho(T)$  measured within the basal plane for both PrAlSi and LaAlSi. Due to, presumably, the atomic disorder between Al and Si sites inherent to these compounds, their residual resistivity ratio  $\rho_{300\text{K}}/\rho_{2\text{K}} \approx 3.8$  is rather small. This appears to be a feature generic to many RAlX family members [11]. Upon cooling from  $T = 300$  K down to approximately 100 K,  $\rho(T)$  of both compounds changes quasilinearly due to the dominating acoustic phonon scattering. Further cooling induces a weak upward bending away from linearity around 50 K for PrAlSi, whereas  $\rho(T)$  of the nonmagnetic compound LaAlSi flattens out below this temperature. The magnetic contribution,  $\rho_m$ , estimated by subtracting the resistivity of LaAlSi from that of PrAlSi, reveals a weak temperature dependence at  $T > T_C$  except for the broad hump around 50 K. Without clear  $-\ln T$  dependence characteristic of Kondo effect, this broad hump is most probably derived from CEF effect, which will be further corroborated by the results of specific heat. Accordingly, the

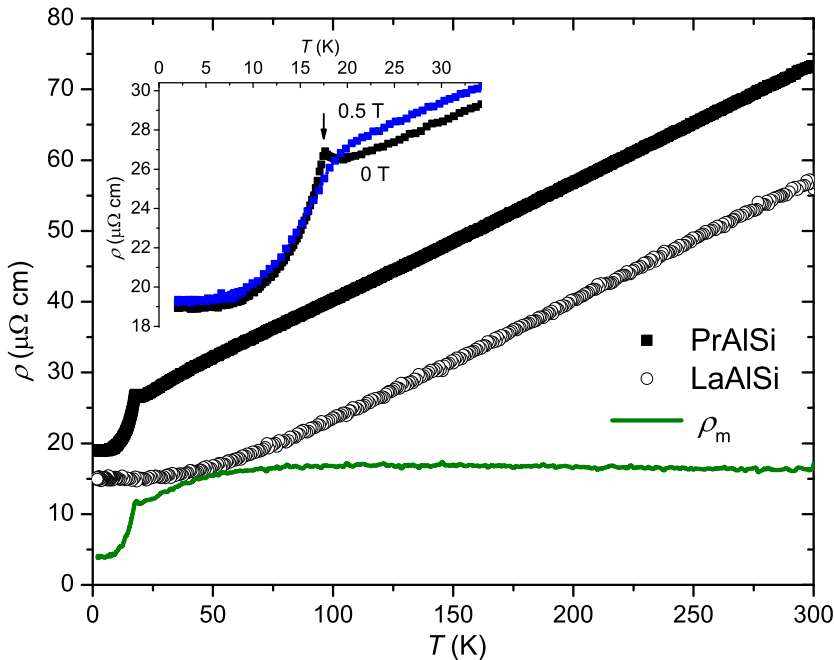


FIG. 5. Temperature-dependent resistivity  $\rho(T)$  of PrAlSi and its nonmagnetic analog LaAlSi. The magnetic contribution  $\rho_m(T)$  is estimated by subtracting the  $\rho(T)$  values of the latter compound from the former. Inset shows an enlarged view of the low- $T$  resistivity, where a clear cusp can be seen at  $T \approx T_C$  for the zero-field measurement. Application of a small magnetic field ( $B = 0.5$  T) smears out this feature.

inverse susceptibility  $1/\chi$  deviates from the Curie-Weiss law below  $T \approx 50$  K, too, see Fig. 2(b).

$\rho(T)$  of PrAlSi does not simply drop at  $T_C$  as is generally expected for local-moment-based metallic ferromagnets. Instead, it starts to increase slightly above  $T_C$  and develops a small cusp (Fig. 5 inset) before decreasing upon further cooling. The cusp at  $T_C$  is field sensitive and can be easily suppressed by a small field (e.g.,  $B = 0.5$  T) applied along the  $c$  axis. We found such resistivity behavior is rather common for FM semimetals with low charge-carrier density and has been observed in, for example, EuCuP (Ref. [27]) and EuB<sub>6</sub> (Ref. [28]). So far, this behavior has been interpreted in two alternative scenarios specific to magnetic semimetals: One relies on the critical spin fluctuations near the magnetic phase transition [29] and the other is based on the formation of magnetic polaron [30].

Figure 6(a) displays the isothermal magnetoresistivity (MR)  $\rho(B)$  measured in transverse magnetic fields ( $I \perp c$ ,  $B \parallel c$ ) for PrAlSi. At  $T < T_C$ ,  $\rho(B)$  first weakly decreases with field (namely, a negative change of MR) until the critical field  $B_c$ , see Fig. 6(b) for a comparison of  $\rho(B)$  and  $M(B)$  for  $T = 2$  K. At  $B > B_c$ , where FM phase is recovered,  $\rho(B)$  becomes a positive function and increases quasilinearly up to at least  $B = 9$  T, see Figs. 6(a) and 6(b). The negative change of MR below  $B_c$  is due to spin disorder scattering and is a generic feature of spin glass [31]. The nonsaturating behavior of  $\rho(B)$  above  $B_c$  is observed all the way up to room temperature, characteristic of a compensated semimetal with small Fermi pockets, in line with the results of Hall-effect measurements to be shown below. At 300 K, the MR ratio defined as  $(\rho_B - \rho_{0T})/\rho_{0T}$  amounts to 40% for  $B = 9$  T, even surmounting that of some typical topological semimetals [32].

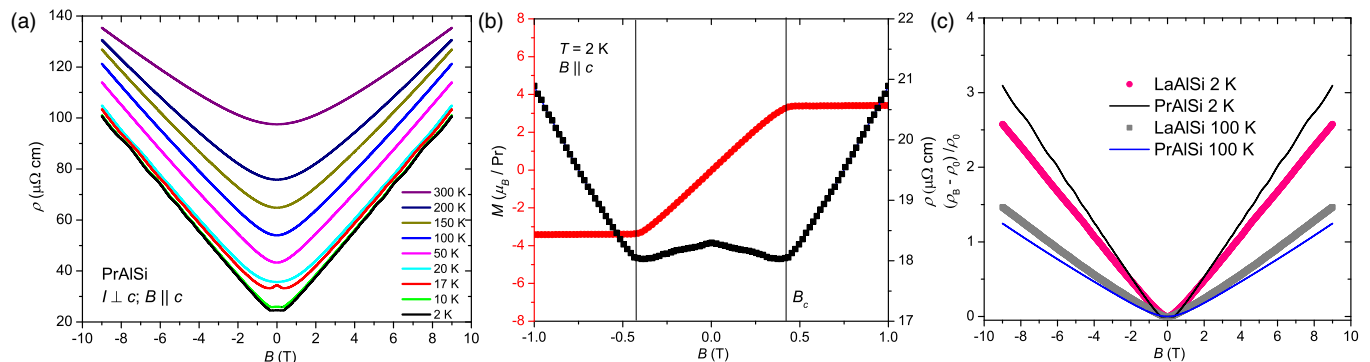


FIG. 6. (a) Isothermal magnetoresistivity  $\rho(B)$  of PrAlSi measured at varying temperatures between  $T = 2$  and 300 K. Below  $T_C = 17.8$  K and in low magnetic fields  $B < B_c$ , MR is only weakly field dependent and slightly negative, see panel (b) for the closeup of  $\rho(B)$  for  $T = 2$  K. At  $B > B_c$ , MR becomes positive and reveals a nonsaturating, nearly field-linear behavior up to 9 T. Magnetic quantum oscillations are also observed below  $\sim 25$  K for PrAlSi. (b) Comparison of low-field  $\rho(B)$  and  $M(B)$  curves measured at  $T = 2$  K. The critical field  $B_c$  observed in both quantities agrees very well. (c) Comparison of the magnetoresistivity ratio  $(\rho_B - \rho_0)/\rho_0$  between PrAlSi and LaAlSi at two selected temperatures,  $T = 2$  K and 100 K. While the magnitude of MR is similar for the two compounds, only the magnetic compound PrAlSi shows clear SdH oscillations at low temperatures. No SdH oscillations can be confirmed for LaAlSi.

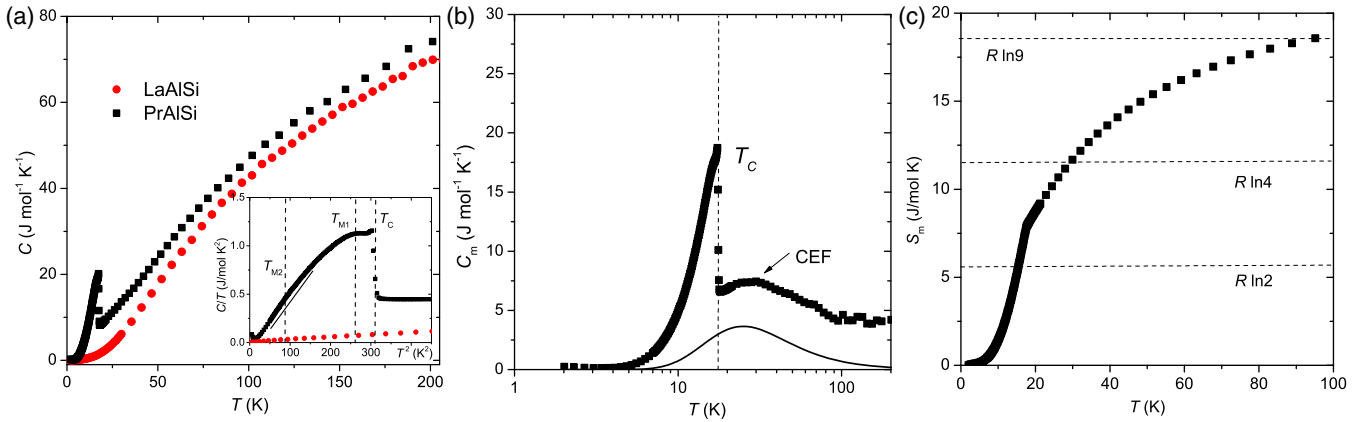


FIG. 7. (a) Specific heat as a function of temperature for PrAlSi and LaAlSi. In addition to the  $\lambda$ -type peak observed at  $T_C$ , a broad shoulder at  $T \approx T_{M1}$  and a weak feature at  $T \approx T_{M2}$  (highlighted by comparing to the straight line) are also visible, see inset. (b) Magnetic contribution to the specific heat,  $C_m$ , estimated by subtracting the specific heat of LaAlSi from that of PrAlSi, is plotted as a function of temperature. A Schottky maximum due to CEF splitting of the  $\text{Pr}^{3+}$  multiplets appears at about 30 K, a temperature rather close to  $T_C$ . To estimate the overall CEF splitting energy, a solid line calculated simply from a ground state doublet and an excited doublet at 60 K is also shown. (c) Magnetic entropy  $S_m$ , obtained by integrating  $C_m/T$  with respect to  $T$ , is shown as a function of temperature.

At temperatures below about 20 K, SdH quantum oscillations are observed for PrAlSi down to a relatively small field  $B \approx 3$  T [Fig. 6(a)]. This clearly manifests the small Fermi pocket of this compound. In Fig. 6(c), we compare the MR ratio of PrAlSi and LaAlSi measured at two representative temperatures,  $T = 2$  and 100 K. Interestingly, no SdH quantum oscillations can be confirmed for LaAlSi in the parameter range down to 2 K and up to 9 T, despite similar MR ratios of the two compounds. These facts suggest that the onset of FM order in PrAlSi has a profound influence on its electronic structure. The SdH quantum oscillations and their unusual temperature dependence will be analyzed below as reflecting an emerging Fermi pocket in the ordered state of PrAlSi.

#### D. Specific heat

Figure 7(a) shows the temperature-dependent specific heat  $C(T)$  for both PrAlSi and LaAlSi. A sharp  $\lambda$ -type peak at  $T_C = 17.8$  K is observed for PrAlSi, with its tail interrupted by a weak shoulder at  $T \approx 16$  K, see Fig. 7(a) inset, where the low-temperature specific heat is plotted as  $C/T$  vs  $T^2$ . The latter temperature value agrees reasonably to  $T_{M1}$  determined by susceptibility (Figs. 2 and 3), indicating a bulk nature of the weak phase transition at  $T_{M1}$ . Likewise, a broad feature at  $T_{M2}$  can also be weakly discerned from the  $C/T(T^2)$  plot. Moreover, a  $C/T$  upturn below 3 K is observed, see Fig. 7(a) inset. This feature appears robust in magnetic field up to at least 9 T (not shown), ruling out residual entropy associated with magnetic frustration and additional magnetic phase transition as the origin. We ascribe this low-temperature upturn to the nuclear Schottky contribution, as has been discussed for FM PrAl<sub>2</sub> (Ref. [33]). Specifically, it is caused by energy splitting of the Pr nuclear spin states ( $I = 5/2$ ) in the internal magnetic field of  $4f$  electrons.

In Fig. 7(b), the magnetic contribution to specific heat,  $C_m(T)$ , obtained by subtracting  $C(T)$  of the nonmagnetic reference LaAlSi from that of PrAlSi, is displayed. Remarkably,  $C_m(T)$  reveals a broad maximum at  $T \sim 30$  K, on which sits

the sharp peak of the FM transition. Note that the two features are rather close in temperature, among which the broad  $C_m(T)$  maximum is a Schottky contribution arising from the CEF splitting of the  $\text{Pr}^{3+}$  multiplets. To shed light on the CEF scheme, the magnetic entropy estimated by integrating the values of  $C_m/T$  with respect to  $T$  is shown in Fig. 7(c). Here, the small portion of the magnetic entropy below  $T = 2$  K, the lowest temperature of our measurements, is ignored. The estimated entropy  $S_m$  at  $T_C$  amounts to 7.9 J/mol K, substantially larger than  $R \ln 2$  (5.76 J/mol K), i.e., the magnetic entropy associated with a doublet ground state but is much smaller than  $R \ln 4$ . Apparently, the magnetic entropy released below  $T_C$  is largely influenced by the broad Schottky contribution centered at 30 K. If the latter is smoothly extrapolated to below  $T_C$  and subtracted from  $C_m(T)$ , the estimated magnetic entropy at  $T_C$  will match reasonably well with  $R \ln 2$ . The ground state of PrAlSi is therefore concluded to be a non-Kramers magnetic doublet, in view of the  $4f^2$  configuration of  $\text{Pr}^{3+}$  ion.

Within the  $\alpha$ -ThSi<sub>2</sub>-type structure, the  $\text{Pr}^{3+}$  ions in PrAlSi adopt the  $D_{2d}(-42m)$  point symmetry. The corresponding CEF will split the  $J = 4$  multiplets into five singlets and two non-Kramers doublets, as was discussed for PrSi<sub>2</sub> [34]. The fact that the full magnetic entropy of the ninefold multiplets ( $R \ln 9$ ) is released at 100 K [see Fig. 7(c)] indicates that all the excited CEF states locate within this relatively narrow energy window. In order to provide a further estimate to the overall splitting energy, in Fig. 7(b), we show a simple calculation of the CEF contribution (solid line) based on a ground state doublet and an excited doublet at  $\Delta = 60$  K, see Ref. [34] for the calculation procedure. As can be observed, this line qualitatively reproduces the observed  $C_m(T)$  maximum at  $T \sim 30$  K and accounts for the large and nearly constant values of  $C/T$  above  $T_C$  [Fig. 7(a) inset]. Therefore, this  $\Delta$  value can be considered a proper energy scale of the center of gravity of the overall CEF excitations, though the detailed energy scheme is yet to be clarified. Related to the weak CEF splitting in PrAlSi, we have recently observed an enhanced

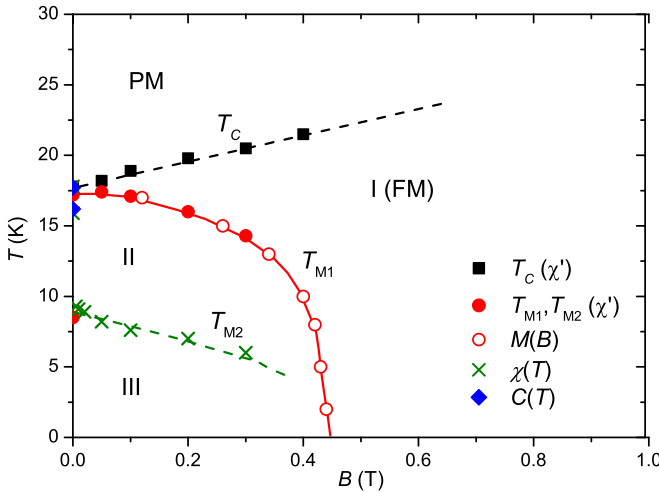


FIG. 8. Temperature-field magnetic phase diagram of PrAlSi. The FM transition temperature  $T_C$  slightly shifts upward in magnetic field, yielding an extended FM phase in field (I). By contrast, the two weak phase transitions at  $T_{M1}$  and  $T_{M2}$  are gradually suppressed by the application of magnetic field, leading to two closed magnetic glassy phases in the low-field low-temperature corner, labeled as II and III.

magnetocaloric effect in this compound which is attributed to the cooperative thermodynamics of the ferromagnetism and CEF effect [35].

### E. Magnetic phase diagram

The magnetic phase diagram of PrAlSi derived from the aforementioned experiments for  $B \parallel c$  is shown in Fig. 8. As revealed by ac susceptibility shown in Figs. 3(e) and 3(f),  $T_C$  shifts slightly upwards with increasing field. Actually, the FM phase transition is still visible in a magnetic field of 5 T at a higher temperature of  $\sim 25$  K (Ref. [18]). In zero field and at  $T < T_C$ , there are two reentrant, weak magnetic transitions at  $T_{M1} \simeq 16.5$  K and  $T_{M2} \simeq 9$  K, below which either FM cluster glass or spin glass takes place. Both  $T_{M1}$  and  $T_{M2}$  can be gradually suppressed by applying magnetic field, forming two closed magnetic phases below  $B_c(T)$  in the low-temperature low-field phase space, denoted as II and III, respectively (Fig. 8). As already mentioned, phases II and III are not canted AFM phases, where the enhanced values of  $\chi''(T)$ , the significant FC-ZFC susceptibility bifurcation, as well as the frequency dependence of ac susceptibility cannot be expected.

To understand the complicated phase diagram composed of FM and reentrant magnetic glassy phases, one should first consider the atomic disorder inherent to this compound, which causes random and/or competing exchange interactions, as has been discussed for  $\text{Mn}_3\text{Sn}$  with glassy ferromagnetism (Ref. [25]). In addition, the low charge-carrier concentration, to be shown below, by which the Ruderman-Kittel-Kasuya-Yosida (RKKY) indirect magnetic exchange interaction is mediated, is another crucial factor that may cause instability of the long-range magnetic order.  $\text{EuB}_6$ , a well-known FM semimetal with multiple magnetic phase transitions, is probably such a case (Refs. [28,36]). The low charge-carrier

concentration or, in other words, the small Fermi energy  $\epsilon_F$  relative to the energy scale of the RKKY magnetic interaction, has been shown to play a dominating role in forming the complicated phase diagram of  $\text{EuB}_6$ . Here, the ferromagnetically ordered state is unstable against spatial fluctuations of carrier concentration and magnetic correlation fixed by the Coulomb interaction of the charge carriers [36].

### F. Normal and anomalous Hall effect

The large anomalous Hall effect in FM and topological materials is being intensively revisited in terms of the enhanced Berry curvature of occupied electronic states [4,37–39]. This issue is of more interest when ferromagnetism and nontrivial band topology coexist, as realized in FM Weyl semimetals [4]. Indeed, in the FM Weyl semimetal candidate  $\text{Co}_3\text{Sn}_2\text{S}_2$ , a sizable anomalous Hall conductivity amounting to above  $1100 \text{ } \Omega^{-1} \text{ cm}^{-1}$  has been observed in the ordered phase [39,40]. Apart from fundamental interest, such effect is attracting increasing attention also because of its potential application in low-energy consumption spintronics [6]. Below, we show an even larger anomalous Hall conductivity for PrAlSi, albeit the absence of Weyl physics at least in zero field.

The experimental results of the Hall-effect measurements are compiled in Fig. 9 for PrAlSi. As seen in panel (a), the Hall resistivity  $\rho_{xy}(B)$  is significantly nonlinear with magnetic field in the temperature ranges both below and above  $T_C$ . It is caused by multiband effect and will be analyzed below along this line. In addition, at  $T < T_C$  and  $B < B_c$ , a linear-in- $B$  contribution to  $\rho_{xy}(B)$ , resembling the corresponding  $M(B)$  curve (Fig. 4), can be recognized. Empirically, the Hall resistivity of a ferromagnet can be expressed as  $\rho_{xy}(B) = \rho_{xy}^N + \rho_{xy}^A$ , the former being the normal Hall resistivity scaling to  $B$  and the latter anomalous one scaling to magnetization, i.e.,  $\rho_{xy}^A = R_S M$  ( $R_S$  is the anomalous Hall coefficient). Based on this description, we can separate the experimental values of  $\rho_{xy}(B)$  at  $T < T_C$  into  $\rho_{xy}^N(B)$  and  $\rho_{xy}^A(B)$ , as demonstrated in Fig. 9(b) for  $T = 2$  K. This is achieved simply by subtracting an estimated  $\rho_{xy}^A(B)$  obtained by scaling to  $M(B)$  to eliminate the kink of  $\rho_{xy}(B)$  at  $B_c$  and to ensure a smooth  $\rho_{xy}^N(B)$ . Because the low-field reentrant magnetic phases (II and III) show magnetic glassy behaviors, no apparent hysteresis loop can be detected in the Hall resistivity  $\rho_{xy}(B)$ , different from the FM semimetal  $\text{Co}_3\text{Sn}_2\text{S}_2$  [39,40].

In Figs. 9(c) and 9(d), we show the isothermal normal Hall conductivity  $\sigma_{xy}^N(B)$  and the anomalous counterpart  $\sigma_{xy}^A(B)$ , calculated from the separated  $\rho_{xy}^N$  and  $\rho_{xy}^A$ , as well as the as-measured values of  $\rho$  and  $\rho_{xy}$ ,

$$\sigma_{xy}^N = \frac{-\rho_{xy}^N}{\rho^2 + \rho_{xy}^2}; \quad \sigma_{xy}^A = \frac{-\rho_{xy}^A}{\rho^2 + \rho_{xy}^2}. \quad (1)$$

One can immediately see that upon cooling into the ordered phase below  $T_C$ , while  $\sigma_{xy}^N(B)$  does not show significant change, large values of  $\sigma_{xy}^A(B)$  emerge rapidly at  $T < T_C$  [Figs. 9(c) and 9(d)].

Figure 9(e) displays the temperature dependence of the anomalous Hall conductivity  $|\sigma_{xy}^A|$ , which is read off  $\sigma_{xy}^A(B)$  at  $B = B_c$  at various temperatures, see Fig. 9(d). For comparison, the as-calculated total Hall conductivity  $|\sigma_{xy}|$  read off at  $B =$

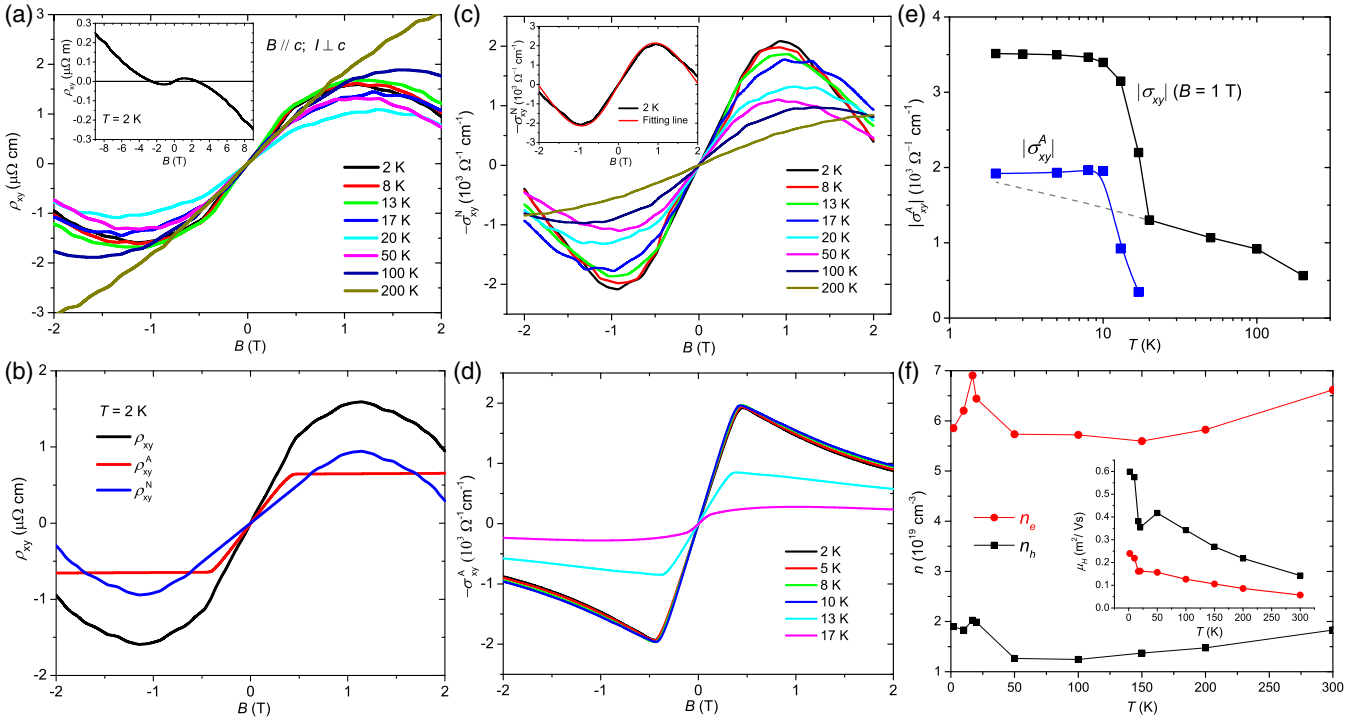


FIG. 9. (a) The Hall resistivity  $\rho_{xy}(B)$ , measured with  $I \perp c$  and  $B \parallel c$ , is shown for a field window  $|B| < 2$  T for varying temperatures. Inset:  $\rho_{xy}(B)$  measured at  $T = 2$  K in a large field range up to 9 T. (b) The measured  $\rho_{xy}(B)$  for 2 K is decomposed into a normal and an anomalous part, assuming  $\rho_{xy} = \rho_{xy}^N + \rho_{xy}^A$ . Among them, the anomalous component  $\rho_{xy}^A$  scales to the magnetization  $M(B)$ , see Fig. 4. Panels (c) and (d) show normal and anomalous Hall conductivities,  $\sigma_{xy}^N(B)$  and  $\sigma_{xy}^A(B)$ , respectively, calculated from  $\rho_{xy}^N(B)$ ,  $\rho_{xy}^A(B)$  and the as-measured resistivity for varying temperatures. Inset of (c) display a two-band fit to the normal Hall conductivity at  $T = 2$  K. (e) Anomalous Hall conductivity  $\sigma_{xy}^A(T)$  read off at  $B = B_c$  from  $\sigma_{xy}^A(B)$  shown in panel (d) and the total Hall conductivity read off at  $B = 1$  T. The dashed line is an extrapolation of the latter value from above  $T_C$ . (f) Carrier concentration  $n$  and Hall mobility  $\mu_H$  (inset) as calculated based on the two-band analysis on  $\sigma_{xy}^N(B)$ , cf. panel (c).

1 T is also shown. Markedly, large values of  $|\sigma_{xy}^A(T)|$  rapidly develop at  $T < T_C$ ; a similar trend can also be seen in the total Hall conductivity  $|\sigma_{xy}(T)|$  as well. On the other hand, the normal Hall coefficient  $|\sigma_{xy}^N(T)|$  changes only smoothly across  $T_C$ , as revealed by the dashed line in Fig. 9(e). The observed  $|\sigma_{xy}^A| \approx 2000 \Omega^{-1} \text{cm}^{-1}$  at  $T < T_C$  is even larger than the giant anomalous Hall conductivity observed in  $\text{Co}_3\text{Sn}_2\text{S}_2$  [39]. We note, however, that the large  $|\sigma_{xy}^A|$  value of PrAlSi is observed at the critical field  $B_c$ . It is not a spontaneous Hall conductivity due to the existence of spin glassy state in zero field, different from that of  $\text{Co}_3\text{Sn}_2\text{S}_2$ . Moreover, a recent work [16] shows that the large anomalous Hall conductivity in PrAlSi is dominated by extrinsic mechanism due to skew scattering, instead of an intrinsic origin determined by Berry curvature.

Assuming a compensated two-band model, the normal Hall conductivity can be expressed in terms of carrier concentrations ( $n_e, n_h$ ) and Hall mobilities ( $\mu_e, \mu_h$ ),

$$\sigma_{xy}^N(B) = \frac{n_e e \mu_e^2 B}{1 + \mu_e^2 B^2} - \frac{n_h e \mu_h^2 B}{1 + \mu_h^2 B^2}. \quad (2)$$

The nonlinear  $\sigma_{xy}^N(B)$  shown in Fig. 9(c) can be well fitted by this model within the field window from  $-2$  T to  $2$  T, see Fig. 9(c) inset for the fitting at  $T = 2$  K. As shown in Fig. 9(f), the estimated carrier concentrations are of the order of  $10^{19} \text{cm}^{-3}$ , which is much lower than that of the typical metals  $\sim 10^{22} - 10^{23} \text{cm}^{-3}$ , characterizing PrAlSi as a semimetal in spite of its

low electrical resistivity. The electronlike carriers have a 3–5 times higher concentration than the holelike carriers; however, the latter show a higher mobility [Fig. 9(f) inset], in line with the positive initial slopes of  $\rho_{xy}(B)$ . In higher magnetic fields ( $B > 4$  T), the electronlike majority carriers dominate and  $\rho_{xy}(B)$  reveals a negative, quasilinear variation with field, see inset of Fig. 9(a).

### G. Shubnikov-de Haas oscillations

As already shown in Figs. 6(a) and 6(c), SdH oscillations are observed in the low-temperature  $\rho(B)$  curves of PrAlSi, but not LaAlSi, in spite of their similar sample quality. The SdH oscillations at  $T = 2$  K are demonstrated in Fig. 10(a). Assuming a smooth, almost  $B$ -linear background (red solid line), the oscillatory part  $\delta\rho(B)$  can be obtained as the difference between the measured  $\rho(B)$  and the smooth background. The consequently obtained  $\delta\rho(B)$  as a function of  $B^{-1}$  is shown in Fig. 10(b) for selected temperatures below 25 K. Clearly,  $\delta\rho(B)$  is a periodic function of  $B^{-1}$  with, however, a significantly  $T$ -dependent periodicity. The fast Fourier transformation (FFT) analysis of the SdH oscillations reveals one dominating frequency for all the temperatures, see Fig. 10(c). Intriguingly, the oscillation frequency changes from  $F = 33$  T at 2 K to  $F = 18$  T at 25 K. The change of  $F$  is not linear in temperature and becomes in particular significant at around  $T_C$ , see Fig. 10(d). It is therefore tempting to relate such

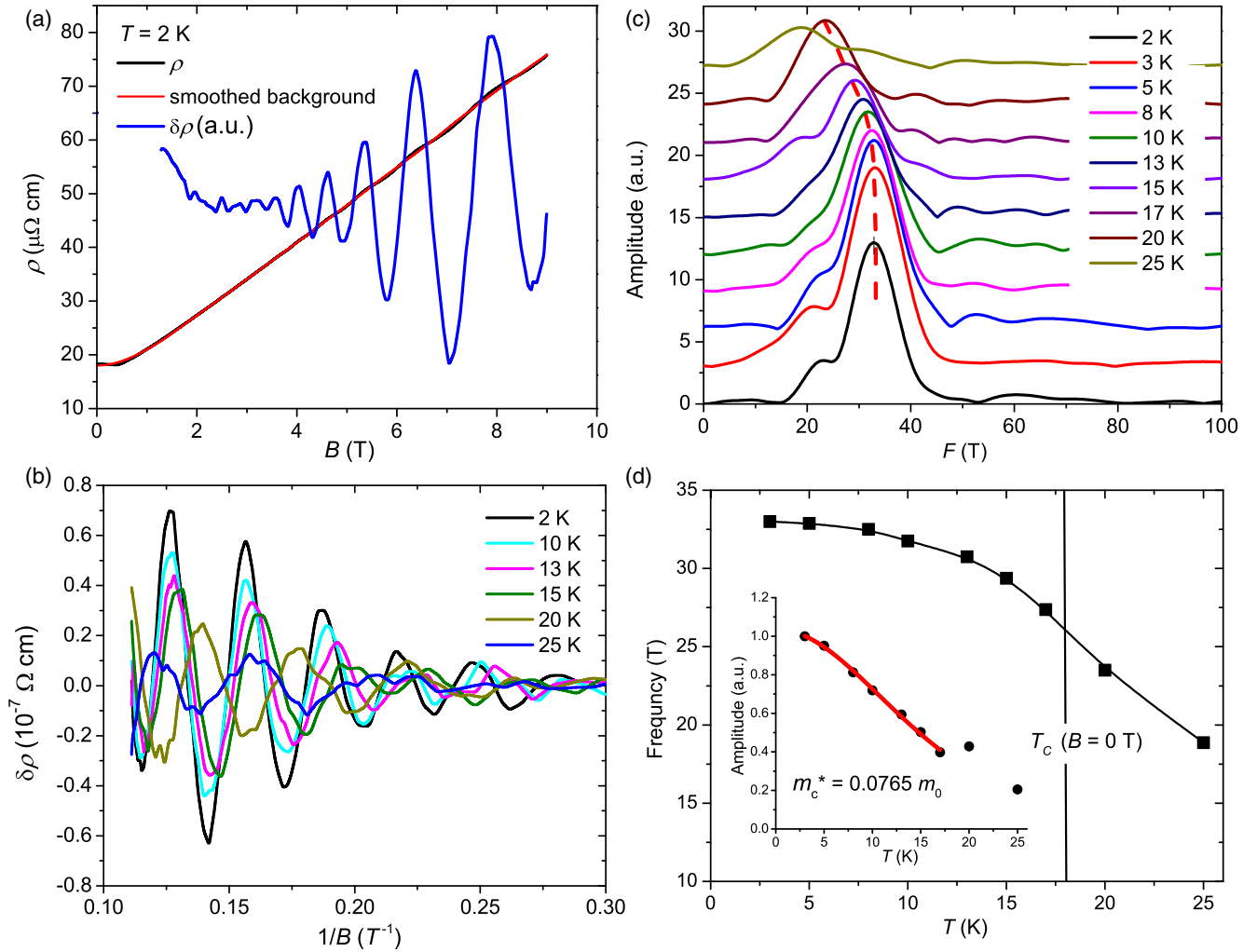


FIG. 10. (a) Magnetoresistivity  $\rho(B)$  measured at  $T = 2$  K in the configuration  $I \perp c$  and  $B \parallel c$  and a smoothed background. Their difference  $\delta\rho(B)$  reveals significant SdH oscillations (blue line).  $\delta\rho(B)$  at  $B < 1$  T is not shown because of the existence of magnetic phase transitions in this field window, see Fig. 8. (b) SdH oscillations at selected temperatures, shown as  $\delta\rho(B)$  vs  $B^{-1}$ . An apparent change of the oscillation period with temperature can be observed. (c) FFT spectrum of the SdH oscillations for selected temperatures below 25 K. The dominating frequency shifts downwards upon warming and the change is particularly significant at  $T \approx T_C$ . (d) Temperature dependence of the SdH oscillation frequency. The vertical line indicates the position of  $T_C = 17.8$  K for  $B = 0$  T, and the actual  $T_C$  in the field interval of the SdH oscillations is several kelvins higher. Inset: SdH oscillation amplitude as a function of temperature. A theoretical fitting for  $T < 17$  K based on the standard Lifshitz-Kosevich theory yields a small cyclotron effective mass  $m^* = 0.0765 m_0$ .

behaviors in PrAlSi to the onset of FM order. Moreover, as revealed by the FFT spectrum, a shoulder appears at the left-hand side of the dominating frequency for all temperatures, see Fig. 10(c). Given the two-band nature as revealed by Hall-effect measurements, this shoulder is likely an intrinsic feature reflecting the Fermi surface of the holelike minority band.

The SdH oscillation frequency is directly proportional to the extremal cross section  $A_F$  of the Fermi surface perpendicular to the magnetic field through the Onsager relation  $F = (\hbar/2\pi e)A_F$ . Naively, the strong temperature dependence of  $F$  observed for PrAlSi indicates a strongly  $T$ -dependent  $A_F$ . Such a change of Fermi surface, by 40% upon warming from  $T = 2$  K to 25 K, is surprising. It is obviously not due to thermal broadening of the Fermi-Dirac distribution, because the Fermi temperature  $T_F$  (i.e.,  $\epsilon_F/k_B$ , with  $\epsilon_F \sim 127$  meV, see below) is far above the temperature window where the

SdH oscillations are observed. Even though still rare, such a strongly temperature-dependent Fermi surface of similar extent has ever been observed for several  $f$ -electron-based semimetals like CeBiPt. There, a temperature-dependent hybridization of the conduction and  $f$  band was argued to be the origin [41]. Contrary to the expectation of this scenario, the estimated cyclotron effective mass of PrAlSi is actually very small, as will be revealed by the  $T$ -dependent oscillation amplitude. Another more likely scenario is that the small Fermi surface is strongly affected by the onset of FM order, i.e., a spin polarization dependent electronic structure. For the rare-earth based FM semimetal EuB<sub>6</sub>, this effect has to be considered in order to interpret its various physical properties like optical conductivity [42,43]. Similarly, the SdH oscillation frequency in FM semimetal Sr<sub>1-y</sub>Mn<sub>1-z</sub>Sb<sub>2</sub> ( $y, z < 0.1$ ) was found to be strongly dependent on the saturated moment [3]. This scenario appears to be reasonable for PrAlSi in

view of the following facts. First, the SdH oscillations are observed only in the magnetic PrAlSi but not the nonmagnetic LaAlSi. Second, the oscillation frequency changes rapidly in the vicinity of  $T_C$ . Here, note that  $T_C$  is an increasing function of field and may increase from  $T_C = 17.8$  K in zero field up to 30 K in the field range of SdH oscillations. This temperature window of  $T_C(B)$  reasonably matches the temperature range where  $F$  strongly changes, see Fig. 10(d).

As shown in Fig. 10(d) inset, by fitting the temperature dependence of the SdH oscillations amplitude at  $T < 17$  K to the temperature damping factor  $R_T = \alpha X / \sinh(\alpha X)$  of the Lifshitz-Kosevich theory, where  $\alpha = 2\pi^2 k_B / e\hbar$  and  $X = m_c^* T / B$ , we have determined the cyclotron effective mass  $m_c^* \approx 0.0765 m_0$ . Here,  $m_0$  is the bare electron mass. Our fitting has been confined to  $T < 17$  K where the oscillation frequency does not significantly change, see Fig. 10(d) inset. The small effective mass and the small Fermi pocket observed for PrAlSi in its ordered state make it easy to probe the quantum oscillations by transport measurements. Based on the Fermi wave vector  $k_F$  determined from  $A_F = \pi k_F^2$  and given that this pocket is dominating in PrAlSi, the Fermi energy  $\epsilon_F = \hbar^2 k_F^2 / m^*$  is estimated to be  $\sim 127$  meV. Note that this value is a rough estimate and will be reduced if one considers the minority band of opposite polarity.

#### IV. SUMMARY AND CONCLUSION

To summarize, we have synthesized single-crystalline samples of PrAlSi and its nonmagnetic reference compound LaAlSi by self-flux method. Single crystal x-ray analysis indicates that PrAlSi adopts the  $\alpha$ -ThSi<sub>2</sub> type structure with random occupation of Al and Si atoms in the identical crystallographic  $8e$  site and has an off-stoichiometric composition, retaining a structure with space-inversion symmetry. Combined dc and ac magnetic measurements on PrAlSi have evidenced not only a FM phase transition at  $T_C = 17.8$  K but also two subsequent reentrant transitions at lower temperatures  $T_{M1}$  and  $T_{M2}$ , below which magnetic glassy behaviors are observed. Due to the strong single-ion CEF, the magnetic moment of Pr<sup>3+</sup> ion is forced to align along the  $c$  axis, in-

dicating Ising-type anisotropy. The reentrant magnetic glassy phases can be easily suppressed by a small magnetic field of  $B_c \sim 0.4$  T applied along the magnetic easy  $c$  axis. In higher magnetic fields of  $B > B_c$ , the FM phase is recovered and a huge anomalous Hall conductivity of  $\sim 2000 \Omega^{-1} \text{cm}^{-1}$  is observed. Moreover, a large, nonsaturating magnetoresistivity appears in both PrAlSi and LaAlSi in wide temperature and field ranges, except for in the spin glassy phases of the former compound.

The SdH oscillations observed in PrAlSi reveal a dominant frequency of 33 T at  $T = 2$  K. Upon increasing temperature to the vicinity of the ferromagnetic transition, both the oscillation amplitude and the oscillation frequency change rapidly and disappear at  $T > 25$  K. By contrast, no SdH oscillations can be observed in LaAlSi in the same temperature and field ranges. These facts naively hint at a magnetic modulation to the electronic structure of PrAlSi upon the onset of the FM order and a consequently emerging small Fermi pocket detected by SdH oscillations. Except for the  $\lambda$ -type peak at  $T_C$ , a broad maximum of magnetic specific heat can be observed in its vicinity at around 30 K. The latter feature can be ascribed to the CEF splitting of the ninefold Pr<sup>3+</sup> multiplets, with a rather small overall energy scale of less than 100 K. These results show that PrAlSi is a new model system of magnetic semimetal where the small Fermi pocket of low electron mass is significantly coupled to local-moment magnetism. For this reason, PrAlSi appears suited for investigating the instability of the RKKY-type magnetic coupling mediated by conduction electrons in a low charge-carrier concentration semimetal. Whether Weyl nodes appear in the time-reversal symmetry breaking FM phase of PrAlSi remains an interesting question.

#### ACKNOWLEDGMENTS

The authors thank the fruitful discussions with F. Steglich, Q. Si, Y.-f. Yang, and J. L. Luo. This work was supported by the National Science Foundation of China (Grants No. 11774404 and No. 11974389), the National Key R&D Program of China (Grant No. 2017YFA0303100), and the Strategic Priority Research Program of Chinese Academy of Sciences under Grant No. XDB33000000.

- 
- [1] N. P. Armitage, E. J. Mele, and A. Vishwanath, *Rev. Mod. Phys.* **90**, 015001 (2018).
  - [2] H. M. Weng, C. Fang, Z. Fang, B. A. Bernevig, and X. Dai, *Phys. Rev. X* **5**, 011029 (2015).
  - [3] J. Y. Liu, J. Hu, Q. Zhang, D. Graf, H. B. Cao, S. M. A. Radmanesh, D. J. Adams, Y. L. Zhu, G. F. Cheng, X. Liu, W. A. Phelan, J. Wei, M. Jaime, F. Balakirev, D. A. Tennant, J. F. DiTusa, I. Chiorescu, L. Spinu, and Z. Q. Mao, *Nat. Mater.* **16**, 905 (2017).
  - [4] A. A. Burkov, *J. Phys.: Condens. Matter* **27**, 113201 (2015).
  - [5] X. Zhang, S. von Molnár, Z. Fisk, and P. Xiong, *Phys. Rev. Lett.* **100**, 167001 (2008).
  - [6] L. Šmejkal, T. Jungwirth, and J. Sinova, *Phys. Status Solidi RRL* **11**, 1700044 (2017).
  - [7] J. Fujioka, R. Yamada, M. Kawamura, S. Sakai, M. Hirayama, R. Arita, T. Okawa, D. Hashizume, M. Hoshino, and Y. Tokura, *Nat. Commun.* **10**, 362 (2019).
  - [8] C. Y. Guo, F. Wu, Z. Z. Wu, M. Smidman, C. Cao, A. Bostwick, C. Jozwiak, E. Rotenberg, Y. Liu, F. Steglich, and H. Q. Yuan, *Nat. Commun.* **9**, 4622 (2018).
  - [9] Y. Xu, C. Yue, H. Weng, and X. Dai, *Phys. Rev. X* **7**, 011027 (2017).
  - [10] G. Chang, B. Singh, S.-Y. Xu, G. Bian, S.-M. Huang, C.-H. Hsu, I. Belopolski, N. Alidoust, D. S. Sanchez, H. Zheng, H. Lu, X. Zhang, Y. Bian, T.-R. Chang, H.-T. Jeng, A. Bansil, H. Hsu, S. Jia, T. Neupert, H. Lin, and M. Z. Hasan, *Phys. Rev. B* **97**, 041104(R) (2018).
  - [11] H. Hodovanets, C. J. Eckberg, P. Y. Zavalij, H. Kim, W.-C. Lin, M. Zic, D. J. Campbell, J. S. Higgins, and J. Paglione, *Phys. Rev. B* **98**, 245132 (2018).
  - [12] P. Puphal, C. Mielke, N. Kumar, Y. Soh, T. Shang, M. Medarde, J. S. White, and E. Pomjakushina, *Phys. Rev. Mater.* **3**, 024204 (2019).

- [13] B. Meng, H. Wu, Y. Qiu, C. Wang, Y. Liu, Z. Xia, S. Yuan, H. Chang, and Z. Tian, *APL Mater.* **7**, 051110 (2019).
- [14] S.-Y. Xu, N. Alidoust, G. Chang, H. Lu, B. Singh, I. Belopolski, D. S. Sanchez, X. Zhang, G. Bian, H. Zheng, M.-A. Husanu, Y. Bian, S.-M. Huang, C.-H. Hsu, T.-R. Chang, H.-T. Jeng, A. Bansil, T. Neupert, V. N. Strocov, H. Lin, S. Jia, and M. Z. Hasan, *Sci. Adv.* **3**, e1603266 (2017).
- [15] T. Suzuki, L. Savary, J.-P. Liu, J. W. Lynn, L. Balents, and J. G. Checkelsky, *Science* **365**, 377 (2019).
- [16] H.-Y. Yang, B. Singh, B. Lu, C. Y. Huang, F. Bahrami, W.-C. Chiu, D. Graf, S.-M. Huang, B. Wang, H. Lin, D. Torchinisky, A. Bansil, and F. Tafti, *APL Mater.* **8**, 011111 (2020).
- [17] A. M. Guloy and J. D. Corbett, *Inorg. Chem.* **30**, 4789 (1991).
- [18] A. L. Lima Sharma, S. Bobev, and J. L. Sarrao, *J. Magn. Magn. Mater.* **312**, 400 (2007).
- [19] H. Flandorfer, D. Kaczorowski, J. Gröbner, P. Rogl, R. Wouters, C. Godart, and A. Kostikas, *J. Solid State Chem.* **137**, 191 (1998).
- [20] S. Bobev, P. H. Tobash, V. Fritsch, J. D. Thompson, M. F. Hundley, J. L. Sarrao, and Z. Fisk, *J. Solid State Chem.* **178**, 2091 (2005).
- [21] S. K. Dhar and S. M. Patalwar, *J. Magn. Magn. Mater.* **152**, 22 (1996).
- [22] M. B. Maple, Z. Henkie, W. M. Yuhasz, P.-C. Ho, T. Yanagisawa, T. A. Sayles, N. P. Butch, J. R. Jeffries, and A. Pietraszko, *J. Magn. Magn. Mater.* **310**, 182 (2007).
- [23] A. A. Belik, N. Tsujii, Q. Huang, E. Takayama-Muromachi, and M. Takano, *J. Phys.: Condens. Matter* **19**, 145221 (2007).
- [24] H. Maletta and W. Felsch, *Z. Physik B* **37**, 55 (1980).
- [25] W. J. Feng, D. Li, W. J. Ren, Y. B. Li, W. F. Li, J. Li, Y. Q. Zhang, and Z. D. Zhang, *Phys. Rev. B* **73**, 205105 (2006).
- [26] M. Balanda, *Acta Phys. Pol. A* **124**, 964 (2013).
- [27] W. Iha, M. Kakihana, S. Matsuda, F. Honda, Y. Haga, T. Takeuchi, M. Nakashima, Y. Amako, J. Gouchi, Y. Uwatoko, M. Hedo, T. Nakama, and Y. Ōnuki, *J. Alloy Comp.* **788**, 361 (2019).
- [28] S. Süllow, I. Prasad, M. C. Aronsen, J. L. Sarrao, Z. Fisk, D. Hristova, A. H. Lacerda, M. F. Hundley, A. Vigliante, and D. Gibbs, *Phys. Rev. B* **57**, 5860 (1998).
- [29] M. Kataoka, *Phys. Rev. B* **63**, 134435 (2001).
- [30] U. Yu and B. I. Min, *Phys. Rev. Lett.* **94**, 117202 (2005).
- [31] J. Pérez, J. García, J. Blasco, and J. Stankiewicz, *Phys. Rev. Lett.* **80**, 2401 (1998).
- [32] M. N. Ali, J. Xiong, S. Flynn, J. Tiao, Q. D. Gibson, L. M. Schoop, T. Liang, N. Haldolaarachchige, M. Hirschberger, N. P. Ong, and R. J. Cava, *Nature (London)* **514**, 205 (2014).
- [33] A. K. Pathak, D. Paudyal, Y. Mudryk, K. A. Gschneidner, Jr., and V. K. Pecharsky, *Phys. Rev. Lett.* **110**, 186405 (2013).
- [34] S. K. Dhar, *J. Magn. Magn. Mater.* **132**, 149 (1994).
- [35] M. Lyu, Z. Wang, K. R. Kumar, H. Zhao, J. Xiang, and P. Sun, *J. Appl. Phys.* **127**, 193903 (2020).
- [36] I. Ya. Korenblit, *Phys. Rev. B* **64**, 100405(R) (2001).
- [37] N. Nagaosa, J. Sinova, S. Onoda, A. H. MacDonald, and N. P. Ong, *Rev. Mod. Phys.* **82**, 1539 (2010).
- [38] H. Chen, Q. Niu, and A. H. MacDonald, *Phys. Rev. Lett.* **112**, 017205 (2014).
- [39] E. K. Liu, Y. Sun, N. Kumar, L. Muechler, A. L. Sun, L. Jiao, S. Y. Yang, D. F. Liu, A. J. Liang, Q. N. Xu, J. Kroder, V. Suss, H. Borrmann, C. Shekhar, Z. S. Wang, C. Y. Xi, W. H. Wang, W. Schnelle, S. Wirth, Y. L. Chen, S. T. B. Goennenwein, and C. Felser, *Nat. Phys.* **14**, 1125 (2018).
- [40] Q. Wang, Y. Xu, R. Lou, Z. Liu, M. Li, Y. Huang, D. Shen, H. Weng, S. Wang, and H. Lei, *Nat. Commun.* **9**, 3681 (2018).
- [41] G. Goll, J. Hagel, H. v. Löhneysen, T. Pietrus, S. Wanka, J. Wosnitza, G. Zwircknagl, T. Yoshino, T. Takabatake, and A. G. M. Jansen, *Europhys. Lett.* **57**, 233 (2002).
- [42] J. Kim, Y.-J. Kim, J. Kuneš, B. K. Cho, and E. J. Choi, *Phys. Rev. B* **78**, 165120 (2008).
- [43] J. Kuneš and W. E. Pickett, *Phys. Rev. B* **69**, 165111 (2004).